Journal of Applied Physics

RESEARCH ARTICLE | OCTOBER 23 2024

Multi-stage precipitation modeling for AA 7050 hole repairs in additive friction stir deposition

Bill Feng ; Manoj R. Rajanna; Jim Lua; Greg Hahn ; Kendall Knight ; Gabriel Murray ; Alan Timmons; Nam Phan

J. Appl. Phys. 136, 165102 (2024)
https://doi.org/10.1063/5.0221890

AIP Publishing

Journal of Applied Physics ARTICLE pubs.aip.org/aip/jap

Multi-stage precipitation modeling for AA 7050 hole repairs in additive friction stir deposition

Cite as: J. Appl. Phys. **136**, 165102 (2024); doi: 10.1063/5.0221890
Submitted: 4 June 2024 · Accepted: 30 September 2024 ·
Published Online: 23 October 2024

Bill Feng,[1,a)] Manoj R. Rajanna,[1] Jim Lua,[1] Greg Hahn,[1,2] Kendall Knight,[2] Gabriel Murray,[3] Alan Timmons,[3] and Nam Phan[3]

AFFILIATIONS

[1]Global Engineering & Materials, Inc., Princeton, New Jersey 08540, USA
[2]Department of Materials Science and Engineering, Virginia Tech, Blacksburg, Virginia 24061, USA
[3]Structures Division, Naval Air Systems Command (NAVAIR), Patuxent River, Maryland 20670, USA

[a)]**Author to whom correspondence should be addressed:** bfeng@gem-innovation.com

ABSTRACT

A multi-stage precipitation model is formulated to predict the microstructural evolution and explain the high performance of additive friction stir deposited aluminum alloy 7050 (AA 7050) for hole repair. The first stage is the heating process due to the high-temperature thermomechanical process of the stir. In this process, small η precipitates dissolve as they lose their stability with increasing temperature, and this causes the volume fraction of η precipitates to decrease and the concentration of Mg and Zn in the matrix to increase. The second stage is the cooling process at the end of the repair where material feeding ends and the tool is lifted away. Heterogeneous nucleation of η precipitates may occur and as the temperature cools below 250 °C, Guinier–Preston (GP) zones start to form. The final stage is the natural aging process, where the η' precipitate starts to grow. The volume fraction and precipitate radius are predicted for each type of precipitate. Furthermore, the fine η' precipitates and GP zones with a decent volume fraction improve the material strength and fatigue life.

I. INTRODUCTION

7xxx series aluminum alloys (AA 7xxx) are precipitation hardening Al–Zn–Mg (–Cu) alloys, with a wide range of applications in the aerospace and space industries, owing to their low density, high strength, good machinability, and decent fracture and fatigue properties. The high strength 7xxx series typically used in aircraft structures are traditionally produced by ingot metallurgy. This process is characterized by melting and alloying, casting into a large ingot that cools relatively slowly, homogenizing the ingot, and fabricating the desired products by thermomechanical means (i.e., rolling, forging, and extrusion).[1] Removing material by milling, machining, carving, shaping, or other means is often necessary. Most recently, additive manufacturing uses computer-aided design software or 3D object scanners to direct hardware to deposit materials, layer by layer, in precise geometric shapes. In many cases, additive manufacturing can provide products with improved material performance, complex geometries, and simplified manufacturing. Today's mainstream metal additive manufacturing technologies (e.g., selective laser melting, electron beam melting, wire arc additive manufacturing, and laser engineered net shaping) are based on melting and rapid solidification, which inevitably leads to hot cracking problems in 7xxx Al alloys that are known as "non-weldable."[2] Additive friction stir deposition (AFSD) stands out as a promising approach that does not require the melting of materials and forms cohesive solid-state bonding between the feed material and the base material during plastic deformation at elevated temperatures. In the AFSD process, the feed material in the form of a rod is stored inside a hollow, cylindrical tool, as shown in Fig. 1. The feed rod rotates with the tool while being pushed onto the substrate simultaneously during the deposition process. The feed material first bonds with the substrate and then spreads across the rotating tool shoulder to form the deposit zone. The tool traverses at the substrate plane to direct the material deposition in a layer-by-layer manner. The solid-state deposition process naturally avoids the defects associated with the melting and solidification in fusion-based additive manufacturing methods, such as powder bed fusion and direct energy deposition. In 2017, AFSD was first introduced by Rivera *et al.* and it provided a new pathway for solid-state additive manufacturing of

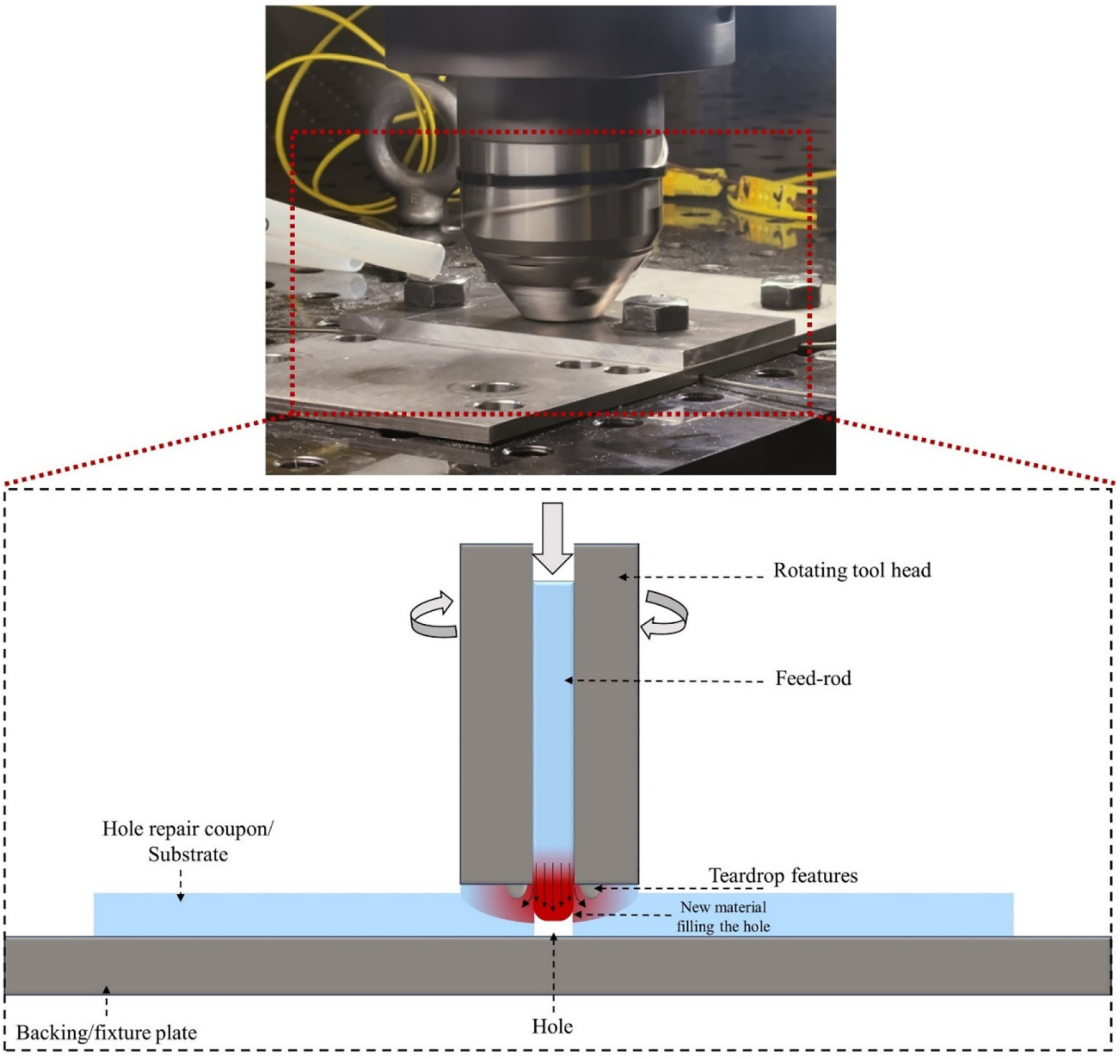

FIG. 1. Illustration of the AFSD process.

Inconel 625.[3] More recently, AFSD has been applied to AA 7xxx materials. Griffiths *et al.* explored the use of AFSD for the repair of volume damage through holes and grooves in AA 7075.[4] Avery *et al.* investigated the microstructural evolution and fatigue mechanisms of an Al–Zn–Mg–Cu alloy (AA7075) manufactured via AFSD.[5] Mason *et al.* studied the influence of the process parameters on the microstructural evolution and mechanical response of a fully dense AA7050 component produced by AFSD. A closed-loop PID temperature control of AFSD was shown to be successful in the deposition of AA 7050-7451, which was compared with a fixed RPM deposition.[10] Forging-like tensile properties were achieved in AFSD fabricated from AA7050 without chemical modification.[7]

When 7xxx series aluminums are used on aircraft, localized regions of damage or corrosion are typical and may negatively affect the lifetime of a component. Typically, these damaged regions are caused by loading or corrosion heterogeneities. In the case of localized damage, a corresponding local repair strategy may be necessary to repair the damaged area and fill it with new material instead of replacing the entire large part. Corroded fastener holes are of particular importance, in-service fastener holes wear due to localized corrosion, contact with a fastener, or stress concentration. The wear of a fastener hole may cause failure of an entire part or assembly, and, therefore, there is a large need to effectively repair fastener holes while maintaining the fatigue lifetime of components. The schematics of the AFSD enabled repair for the damaged or corroded hole coupons can be seen from Fig. 2. Our recent experiment shows that depositing AA7050-T7451 via AFSD as a repair for a simulated fastener hole in AA7050-T7451 creates a structural repair with improved fatigue life.[8] This increase in fatigue life has been explained by the reduction in size and aspect ratio of the Fe-rich

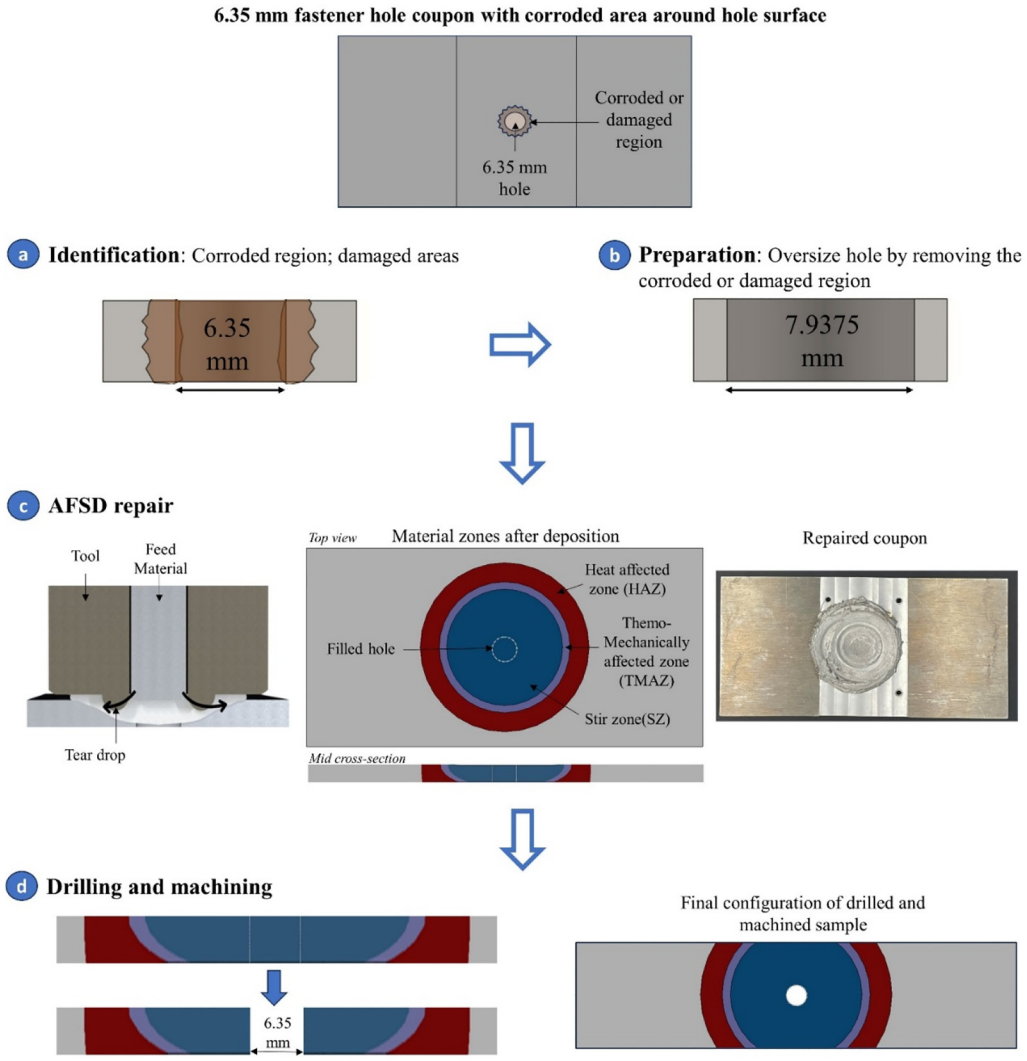

FIG. 2. Schematic of the different steps in AFSD-enabled repair for fastener hole coupons with corroded regions. (a) Identification: the corroded or damaged region is identified in a fastener hole coupon (the original fastener hole size is 6.35 mm in diameter). (b) Preparation: the coupon is prepared for repair by oversizing the hole to remove the corroded region. The new hole diameter is increased to 7.9375 mm, assuming the corroded or damaged part is within this size. (c) AFSD repair: the hole is filled using additive friction stir deposition (AFSD) to obtain a repaired coupon. This process involves the deposition of new material into the hole, which utilizes the proprietary repair process, creating a repaired coupon with distinct material zones: a heat affected zone (HAZ), a thermo-mechanically affected zone (TMAZ), and a stir zone (SZ). (d) Drilling and machining: after the AFSD repair, the filled area is drilled and machined back to the original fastener hole diameter of 6.35 mm, achieving the final configuration as shown in the figure to the right.

constituent particles that serve as crack initiation sites in conventional material during the high shear of AFSD. After AFSD, these constituent particles do not serve as the main crack initiation sites.[8] Since the main strengthening mechanism for AA 7050 is the precipitates, the precipitation evolution serves as another alternative for performance improvement. The fine precipitates directly improve the material strength via Orowan strengthening, impeding the movement of dislocations associated with plastic deformation. The usual precipitation sequence of 7xxx follows the sequence of solid solution (SS) → Guinier–Preston (GP) zones → metastable η' → stable η.[9] GP zones, η', and small-sized η are all treated as strengthening particles, while overgrown particles η may reduce the strength of the material. The size, distribution, and type of the precipitates are highly dependent on the thermal history in AFSD. Proper control of the precipitation in AFSD, particularly control of the size and density of these precipitates, is, therefore, critical to achieving optimum alloy properties. To tailor the processing conditions (such as rotation speed, force, feeding rate, active cooling, etc.),

it would be very useful to have a microstructural model of the precipitate evolution during AFSD to correlate a thermal history to precipitate evolution. In particular, the *in situ* observation of the precipitation process is experimentally inaccessible.

There has been modeling work focused on the AFSD manufactured AA 7xxx materials. A strain rate-dependent plasticity-damage material model was presented for precipitation hardened AA 7050 by AFSD.[10] In order to predict grain and intermetallic sizes within the repaired geometry over a range of AFSD parameters, SPH process modeling with the Zener–Hollomon parameter was developed.[11] A microstructure-sensitive fatigue life model was used to elucidate the process–structure–property fatigue mechanism relations of the heat-treated repair by using AFSD and wrought AA7075.[12] A smooth particle hydrodynamic (SPH) simulation of AFSD repair was used to inform a multi-physics approach to predict the fatigue life of a high-strength aluminum alloy, in which the model predictions were obtained from combinations of SPH thermomechanical simulations, phase field simulation, and a calibrated microstructure sensitive fatigue model.[13] Since the main strengthening mechanism for AA 7050 is the precipitation, the focus of this paper is to model the multi-stage precipitation evolution. One of the powerful tools for modeling the precipitate evolution is the Kampmann and Wagner numerical (KWN) precipitation model.[14] The GP(I) zone formation during quenching is simulated in an AA 7449 75-mm thick plate by using the KWN model;[15] the volume fraction and size of the GP zone are predicted and compared with experimental data.[15,16] Kamp *et al.* modeled the evolution of heterogeneous precipitate distribution during the friction stir welding process, in which the formation of η precipitates on the grain boundaries and homogenous nucleation of η and η' precipitates are considered.[17–19] In addition, the evolution of η and η' precipitates during the AFSD process and heat treatment was predicted using Thermocalc TC-Prisma,[13] where the heterogeneous nucleation of precipitates at the grain boundaries was not considered. There is no work predicting the precipitation in AFSD with three strengthening particles (GP zones, metastable η', and stable η), while they can be found coexisting.[20] In this paper, we model the precipitate evolution in AFSD, where multiple precipitates (GP zones, metastable η', and stable η) at multi-stage evolution at both the matrix and the grain boundaries are considered. This hole filling and repair process may have wide industrial applications. The objective of the present work is to model and explain the precipitation evolution in an AA 7050-T7451 hole repair during AFSD and to further contribute to the understanding of the strengthening mechanism.

II. EXPERIMENT

The experimental procedures and methods summarized in this section for the hole repair process are described in detail in Ref. 8. Figure 2 illustrates an overview of the AFSD enabled repair for the damaged or corroded hole coupons. The feed material and substrate were AA 7050-T7451 from Tri-Tech Metals (Rancho Cucamonga, CA, USA). The substrates were machined from a $76.2 \times 152.4 \times 6.35\ \text{mm}^3$ rolled plate and the center of the substrates was machined to a thickness of 4.0 mm and a 7.9375 mm hole is drilled in the center, which is the preparation stage of the repair process as illustrated in Fig. 2(b). The feed rod was $152.4 \times 9.525 \times 9.525\ \text{mm}^3$ square rods, coated with graphite lubricant to facilitate printing. AFSD was carried out on a MELD R2 system (MELD Manufacturing, Christiansburg, VA, USA). For all prints, a tool with four 2.29 mm high teardrop features in the face was used. To conduct the repairs, a proprietary repair process was utilized, which promotes material mixing between the base material and the deposited material. The example sample after the hole repairs can be found in the right-hand side picture in Fig. 2(c). Microstructural samples were excised from a representative hole repair sample and examined via EBSD and TEM to examine the microstructure. Meanwhile, 20 repaired samples were machined and drilled with a 6.35 mm hole as shown in Fig. 2(d) and subjected to fatigue testing. These were compared to the results for the base pristine materials having the same geometry. It is found that the fatigue life is improved for the AFSD enabled hole repaired samples from the base pristine materials.[8] Specifically, the fatigue life of AFSD repaired coupons with $R = 0.1$ condition with a maximum stress of 478 MPa outperforms the fatigue life of pristine materials, where the fatigue cycle for 60% lifetime is 20 786 in repaired coupon vs 15 836 in the pristine coupon.[8] We noted that experimental fatigue results exhibited significant scatter for AA 7050 pristine and repaired materials in Ref. 8, which could also be found in AA 7050 for the heat-treated AFSD repaired plate in Ref. 12

III. PRECIPITATION PATHWAY IN BASE MATERIALS AND AFSD

7xxx series aluminum alloys have different types of precipitates, and their evolution can be sophisticated. Their size and volume fraction distribution mainly depend on the temperature history and are also affected by the dislocation density, grain boundary density, etc. In this section, we propose the possible pathways for precipitation evolutions in AFSD, which are supported by our TEM results and experiments in the literature.

A. Precipitation in the base materials

Different heat treatments result in different precipitation pathways in the base materials.[21] In Ref. 22, naturally aged and overaged conditions are compared. The precipitate types, volume fractions, and sizes are strongly influenced by the heat treatment processes. Understanding the effects of heat treatment and temperature on precipitation is valuable because the temperature history can be controlled by changing process parameters and with active cooling in AFSD. This can change the precipitation pathways and therefore the material properties and performance.

Over-aging refers to allowing the alloy to age for an extended period at an elevated temperature compared to the optimum aging temperature. The optimum aging temperature is the temperature at which the precipitation of strengthening particles is most efficient, leading to the highest achievable strength for a given alloy. Over-aging occurs when an alloy is aged at a higher temperature or longer than recommended for achieving peak strength. While over-aging can result in further growth and coarsening of the precipitates, it can also reduce the strength gained from the aging process. In the T7 over aging heat treatment, there is a solutionizing treatment followed by quenching. Following quenching, the alloy is

then aged at an intermediate high temperature for a period. Above the GP zone solvus temperature, the η' phase and η phase can heterogeneously nucleate at the grain boundaries or around dispersoids at a faster rate.[1] In the matrix, the η' and η phases form much slower, and there are two alternative formation paths: the first is that large GP zones form first, and then fully transform into η' and η phases, and the second is that η' phase and η phase directly form from solid solutions without GP zones.[15] Since the aging process occurs at an elevated temperature for a long period of time, all η' phases can be transformed into η. Therefore, small angle x-ray scattering (SAXS) data showed that the precipitate in overaged (T79 heat treatment) 7449 Aluminum alloy is the η phase and the GP zone and η' do not exist.[15] For AA 7050-T7451, it is aged using two-stage heat treatment as in T79. After solutionizing, AA 7050-T7451 is heated at 122 °C (250 °F) for 3 to 6h. It is again heated at 163 °C (325 °F) for 15 h followed by air cooling. For this long period of 18–21 h at elevated temperature, all GP zones or η' are transferred to η, and η is the only precipitate considered in the base material of AA 7050-T7451.

B. Precipitation evolution in AFSD

Hole repairs were conducted with a thermocouple embedded within the tool. For the purposes of modeling, this temperature measurement was treated as a representation of the stir zone temperature during heating. After printing was completed, the cooling process was modeled by CFD with the heat transfer solver in STAR-CCM.[23] As shown in Fig. 3, the tool temperature history is from 0 to 203 s and temperature from 203 to 550 s is from the heat transfer model. We are interested in the thermal history of the stir zone for the hole repair geometry because the region contains the potent stress concentrator that serves to initiate the fracture as shown in Fig. 2(d). In the initial overaged base material, there are low levels of Zn and Mg in solution as the alloying elements are contained within the η phase precipitates. In Fig. 3, the heating time is from 0 to 203 s. In this process, the small η precipitates dissolve into the matrix as they lose their stability with increasing temperature. This causes the overall η precipitate volume fraction to decrease, and the concentration of Mg and Zn in the matrix increases. On the contrary, larger particles may grow with the temperature increase. This growth is driven by two factors. First, the concentration of the solute Mg or Zn in the matrix increases due to the dissolving small precipitates. Second, the equilibrium concentration C_i of Mg or Zn at the interface between precipitates and the matrix is a decreasing function of precipitate radius R, and for large radius precipitate η, it grows as long as $C_e > C_i$, where C_e is the equilibrium concentration of Mg or Zn in the matrix. C_e increases with an increase in temperature as shown in Fig. 4. When C_e is larger than the C_i of all particles, all precipitates start to dissolve. At the solvus temperature around 400–450 °C, all η phase in the base material is dissolved into solution. This temperature range corresponds to the stir zone in AFSD or FSW.[24] However, for HAZ and TMAZ zones, precipitates may grow but the total volume fraction of precipitates decreases as the temperature increases. In the heating process, GP zones may not be formed. At a temperature of 100–200 °C, GP zones can form quickly[15,16] but there is little solute at that temperature range. Above 200–250 °C, the nucleation of GP zones is very slow because the change in Gibbs free energy from solution to GP zones reduces at high temperatures. Only large radius GP zones can form (small GP particle is not stable at high temperature). Above 250 °C is above the GP solvus temperature and there are no GP zones.[15] During this heating, homogenous

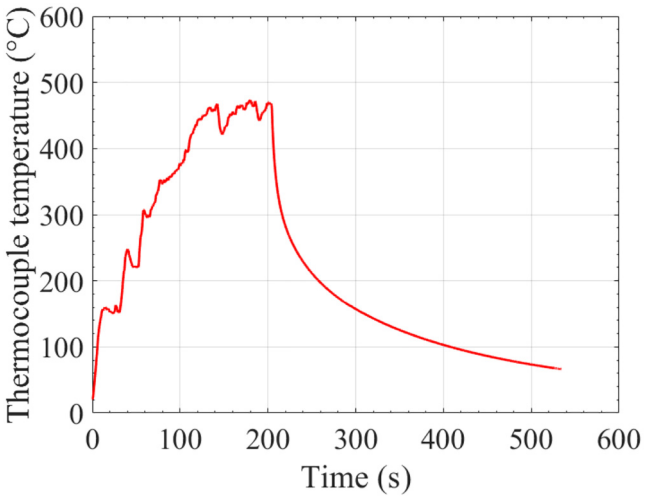

FIG. 3. The temperature history collected from a thermocouple in the AFSD tool (0–203 s) and the CFD model (203–530 s). The thermocouple is embedded in the tool shoulder and it is close to the outer diameter and at the bottom of the shoulder. Our CFD results by STAR-CCM shows that the temperature is very representative to the temperature around the hole of the coupon. For the cooling process, temperature around the hole is obtained from CFD model. The CFD model can be found in Ref. 23.

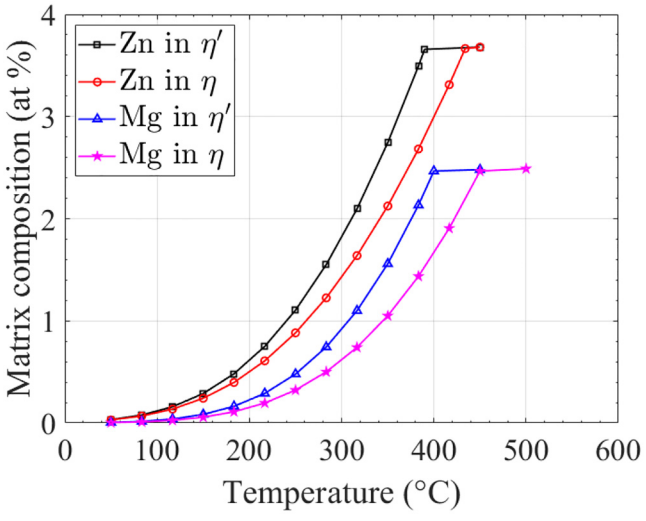

FIG. 4. The solute concentration C_e in the matrix at the equilibrium corresponding to η' and η at different temperatures obtained from the software JMatPro.[19]

nucleation of η' or η phase in the matrix may not occur. Telesman (1984) mentioned that the nucleation of η' can only occur on dislocations, grain boundaries, or dispersoids and at temperatures above the GP solvus.[1] As shown in Fig. 3, that temperature range only lasts for a very short period of time before it reaches the η' or η solvus temperature. The nucleation and growth of the η' precipitate in the matrix takes much longer than this time period so it is not expected to occur. However, heterogeneous nucleation around defects is much easier than growth in the matrix because the defects provide the additional driving force for precipitation evolution and Mg and Zn diffuse faster there. Therefore, heterogeneous nucleation of η' or η may occur during heating before the temperature reaches 400 °C. Above 400 °C, all the η' or η should be all soultionized. The heterogeneous nucleation around the defects is considered to be the η phase only, since the additional driving force and fast solute diffusion may lead to the transition from the matrix to η precipitates without intermediate η' precipitates.[19]

At the cooling stage, the first region of interest is the decrease from the maximum temperature to about 250 °C. In this period of time, GP zones cannot be formed and η heterogeneous nucleation occurs at grain boundaries, dislocations, or dispersoid particles. From 250 to 100 °C at the cooling rate in Fig. 3, the GP zones can form rapidly based on the experimental results in Ref. 15 because the interfacial energy is lower, and the radius is smaller than those in η precipitates. The GP zones in the temperature range of 250 to 100 °C are sub-nanometer in size and must be detected by SAXS as they are too small to be seen by TEM. Large-size GP zones from TEM are found only below 125–100 °C in FSW.[24] Below 100 °C to room temperature and natural aging, the precipitation process occurs very slowly because the solute concentrations of Mg and Zn are low, and the diffusion rate of Mg and Zn decreases at lower temperatures. In the natural aging process, GP zones act to homogeneously nucleate η' and η.

IV. GOVERNING EQUATIONS FOR THREE STAGES OF PRECIPITATION EVOLUTION IN AFSD

A. Heating

The base material is AA 7050-T7451. To achieve the T7451 heat treatment, it is heated at 122 °C (250 °F) for 3–6 h. It is then reheated at 163 °C (325 °F) for 15 h followed by air cooling. During this long period of 18–21 h at an elevated temperature, all GP zones or η' transform into η, and η is the only precipitate in the base material. In this state, there are low levels of Zn and Mg in solution. In AFSD, the temperature increases as the feed rod and tool create frictional heat with the base material. The small precipitates η are stable at low temperatures, while the large ones are stable at high temperatures. In this heating process, the small η precipitates dissolve as they lose their stability with increasing temperature; this causes the overall η precipitate volume fraction to decrease, and the concentration of Mg and Zn in the matrix to increase.

The dissolving rate $v_\eta(R)$ of a precipitate η with radius R due to diffusing element E as in Ref. 25 is given as

$$v_\eta(R) = \frac{dR}{dt} = \frac{D_E}{R}\frac{c_{mE} - c_{RE}^{e/\eta}}{c_{\eta E}^{e} - c_{RE}^{e/\eta}}, \tag{1}$$

with $c_{RE}^{e/\eta}$ being the equilibrium solute mole fraction at the precipitate/matrix interface. $c_{\eta E}^{e}$ is the equilibrium solute mole fraction in the precipitate η. c_{mE} is the concentration of element E in the matrix. Here, the composition of the precipitate is $MgZn_2$ and the element E is either Mg or Zn. The growth rate of Mg or Zn is constrained as in Ref. 19,

$$\frac{D_{Zn}}{R}\frac{c_{mZn} - c_{RZn}^{e/\eta}}{c_{\eta Zn}^{e} - c_{RZn}^{e/\eta}} = \frac{D_{Mg}}{R}\frac{c_{mMg} - c_{RMg}^{e/\eta}}{c_{\eta Mg}^{e} - c_{RMg}^{e/\eta}}. \tag{2}$$

The precipitation sequence of 7XXX series Al alloys in the matrix can be summarized as solid solution (SS) → GP zones → metastable η' → stable η,[9,26] where the Gibbs free energy decreases continuously in this process. However, the interfacial energy between the matrix and the GP zones is smaller than the interfacial energy between matrix and η' or η. The interfacial energy of η' with the matrix is smaller than η with the matrix. To overcome the large interfacial energy between the matrix and η, precipitation typically follows the sequence of solid solution (SS) → GP zones → metastable η' → stable η. This process typically takes longer than the heating time in the AFSD process, and thus the homogeneous nucleation of η or η' does not occur in the matrix during heating. In Ref. 15, when the temperature is cooled from 500 °C to room temperature over the course of a couple of minutes, GP zones are the only precipitates but the η' and η precipitates are almost not found in the matrix. For this reason, precipitation of η' and η is not considered as homogeneous nucleation in the matrix. However, heterogeneous nucleation may occur in the grain boundaries or around the constituent particles.[1] This is because there are many dislocations, voids, and other defects in the grain boundary, which not only provide sufficient energy for precipitation from the matrix into the η phase but also accelerate the diffusion of solute elements.[1] The heterogeneous nucleation of the η phase is introduced below.

Aaron and Aaronson[27] used a simple constant collector plate area model based on equating the solute supply to a grain boundary precipitate with the flux required for a precipitate to grow to a given size. The solute supply is given by dm/dt,

$$\frac{dm}{dt} = A_v D_v \frac{d}{dR}[X(r,t)]_{r=0}, \tag{3}$$

where A_v is the collector plate area, D_v is the volume diffusion coefficient for the solute in the matrix, X is the composition, r is the distance, and t is the time. Since Mg is the slowest solute to diffuse, we only consider the diffusivity of Mg for heterogeneous nucleation.

In Ref. 28, Carolan and Faulkner modifies $\frac{dm}{dt}$ in Eq. (3) by using $\frac{dV}{dt}$ and obtained the expression

$$\frac{dV}{dt} = X \cdot A_v \cdot D_v^{\frac{1}{2}} \cdot t^{-\frac{1}{2}} \cdot \pi^{-\frac{1}{2}}, \tag{4}$$

where V is the volume of precipitate particle and $X = \frac{c_{mMg} - c_{Mg}^{e/\eta}}{c_{\eta Mg}^{e} - c_{Mg}^{e/\eta}}$. $c_{Mg}^{e/\eta}$ is the equilibrium of concentration Mg in the matrix. As can be seen from the expression of X, if the concentration of Mg in the matrix c_{mMg} is greater than $c_{Mg}^{e/\eta}$, the driving force of the matrix to η is positive $\left(\frac{dV}{dt} > 0\right)$. However, the interfacial energy may be the

barrier to this transition. Over a long enough period of time, this transition in the matrix can be completed due to thermal fluctuations. In a few minutes of heating time, this precipitation only occurs heterogeneously at the grain boundary or around constituent particles. Note that we may also define $X = \frac{c_{mMg} - c^{e/\eta}_{RMg}}{c^{e}_{\eta Mg} - c^{e/\eta}_{RMg}}$. In the Kampmann and Wagner numerical (KWN) model, $c^{e/\eta}_{RMg}$ is linear to $c^{e/\eta}_{Mg}$ and increases with a decreasing precipitate particle radius R. This may make the integration of Eq. (4) sophisticated and may introduce a singularity problem as $c^{e/\eta}_{Mg}$ goes to infinity when R goes to zero. For simplicity and to avoid the non-physical $c^{e/\eta}_{RMg}$, only $X = \frac{c_{mMg} - c^{e/\eta}_{Mg}}{c^{e}_{\eta Mg} - c^{e/\eta}_{Mg}}$ is considered as a function of temperature and independent of R. This strategy was taken from Ref. 28, when integrating Eq. (4), they treated X independent of R.

In Eq. (4), the collector plate area A_v can be defined for a circular area around the precipitate, and we can write volume V as a function of R as in Ref. 19,

$$A_v = 4\pi D_b t, \tag{5}$$

$$V = \frac{4}{3} * \pi R^3. \tag{6}$$

Here, D_b is the diffusivity of Mg in the grain boundary, and if we assume $\frac{D_b}{D_v} = k$, Eq. (4) can be rewritten as

$$\begin{aligned} dV = d\left(\frac{4}{3} * \pi R^3\right) &= X \cdot A_v \cdot D_v^{\frac{1}{2}} \cdot t^{-\frac{1}{2}} \cdot \pi^{-\frac{1}{2}} \cdot dt \\ &= 4k \cdot X \cdot D_v^{\frac{3}{2}} \cdot t^{\frac{1}{2}} \cdot \pi^{\frac{1}{2}} \cdot dt. \end{aligned} \tag{7}$$

Similar to Ref. 18, k is chosen to be 16 in our study. The radius of the grain boundary precipitate R can be solved numerically from Eq. (7) by discretizing the time steps into small time increments. Let V_{GBppt} be the total volume of precipitates of one grain and V_{Grain} be the volume of one grain. The volume fraction f_{GBppt} of heterogeneous precipitates η in the grain boundary is given by

$$f_{\mathrm{GBppt}} = \frac{V_{\mathrm{GBppt}}}{V_{\mathrm{Grain}}} = \frac{\frac{4}{3} * \pi R^3 * N_0}{V_{\mathrm{Grain}}}, \tag{8}$$

where N_0 is the number of nucleation sites in a unit grain, and it is reasonable to assume that it is a linear function of grain boundary area A_{GB}:$N_0 = p^* A_{GB}$. p is the number of nucleation sites per unit grain boundary area, and $p = 100$ in this study. In addition, A_{GB} is related to the grain size V_{Grain}, and the following experimental data in Table I may be used.[19] One may use a linear or quadratic interpolation method to determine A_{GB} for grain volume beyond the following three data points. In this study, we directly use the EBSD data of A_{GB} and V_{Grain} from our repaired sample.

TABLE I. The grain boundary area vs grain volume.[19]

A_{GB} (μm^2)	V_{Grain}(μm^3)
8800	48 000
1600	4 000
600	1 000

The mean solute mole fraction in the matrix $\bar{C}$ is expressed as volume fraction of f_{GBppt} and $f_{\mathrm{matrix\_ppt}}$.

$$\bar{C} = \frac{C_0 - C_p(f_{\mathrm{GBppt}} + f_{\mathrm{matrix\_ppt}})}{1 - (f_{\mathrm{GBppt}} + f_{\mathrm{matrix\_ppt}})}, \tag{9}$$

where C_0 is the initial solute content in alloy. Therefore, a fully coupled precipitation process in the matrix and grain boundary is considered.

B. Cooling process

There are two stages in the cooling process: (1) from the maximum temperature to 250 °C and (2) from 250 °C to 100 °C. In the first, higher temperature regime, GP zones cannot be formed. Undissolved η in the matrix may grow and/or heterogeneous nucleation at grain boundaries may occur as governed by the equations discussed during heating. In the second regime, GP zones are formed from 250 to 100 °C, based on the results from Ref. 15 because the interfacial energy is lower and the radius of GP zone is smaller than those in η' and η.

We used the KWN model for GP zone nucleation as well as the growth/dissolving of GP zones. A similar theoretical model is also used in Ref. 25, which gives an excellent prediction for GP zone precipitation due to slow and fast quenching process. From 250 to 100 °C, the governing equations for the GP zones evolution is described below.

In multicomponent systems such as 7xxx series aluminum alloys, a common approximation is to assume that nucleation is controlled by the slowest diffusing element in the precipitates, and in AA 7050, that element is magnesium.[15] This assumption is simpler than the theory described in the heating process but it provides very good agreement between the modeling and experimental results for GP zone evolution during cooling.[15] The nucleation is reduced into the pseudo-binary problem, and the nucleation rate I is given as[25]

$$I = N_0 Z \beta^* e^{\left(\frac{-\Delta G^*}{k_B T}\right)}, \tag{10}$$

where N_0 refers the nucleation site density, Z is the Zeldovich's factor as given by

$$Z = \frac{\Delta G_V^2}{8\pi V_m N_{AV} (\gamma^3 k_B T)^{1/2}}, \tag{11}$$

where k_B is the Boltzmann's constant and T is the temperature in Kelvin. N_{AV} is Avogadro's number.

The frequency factor β^* is the condensation rate of solute atoms in a cluster of critical size R^*, which can be calculated as

$$\beta^* = \frac{4\pi R^{*2} D \bar{C}}{a^4}. \tag{12}$$

The energy barrier ΔG^* in Eq. (10) is defined by the interfacial energy γ and Gibbs free energy ΔG_V^2,

$$\Delta G^* = \frac{16\pi\gamma^3}{3\Delta G_V^2}. \tag{13}$$

The critical radius of nucleation R^* is defined as

$$R^* = -\frac{2\gamma V_m}{\Delta G_V}. \tag{14}$$

We assume that the GP zone is of a spherical shape with radius r and the solute concentration C_p, and it is embedded in a super-saturated solid solution of a mean concentration $\bar{C}$. The growing/dissolving velocity $v(r)$ of a particle can be written as

$$v(r) = \frac{D}{r}\frac{\bar{C} - C_i}{C_p - C_i}, \tag{15}$$

with C_i being the equilibrium solute mole fraction at the precipitate/matrix interface and diffusivity $D = D_0 e^{\left(-\frac{Q_d}{RT}\right)}$: D_0 being the pre-exponential coefficient and Q_d being the activation energy of the diffusion. C_i is related to the equilibrium solute mole fraction in the matrix C_e, via the Gibbs–Thomson equation:

$$C_i = C_e e^{\left(\frac{2\sigma V_m}{rRT}\right)}, \tag{16}$$

in which σ is the particle–matrix interface energy and V_m is the molar volume of the particle.

Solving for the critical radius r^* at the zero velocity in Eq. (15) by combining with Eq. (16) gives

$$r^* = \frac{2\sigma V_m}{RT\ln(\bar{C}/C_e)}. \tag{17}$$

Similar to the diffusion problem, the growth or dissolution of particles that occurs during a small-time increment Δt can be considered as a flux of matter in or out of the elements. Let J denote the particle flux, while N represents the number density of particles within Δr. The conservation of the mass in the system is regulated by the following equation:

$$\frac{dN}{dt} = -\frac{dJ}{dr} + I, \tag{18}$$

where I is the nucleation rate in Eq. (18), and particle flux J through the volume element is given by the following equation:

$$J = N \cdot v(r). \tag{19}$$

The mean solute mole fraction in the matrix $\bar{C}$ is expressed as the volume fraction of precipitates,

$$\bar{C} = \frac{C_0 - C_p f_v}{1 - f_v}, \tag{20}$$

where C_0 is the initial solute content in alloy and the volume fraction of particles f_v can be computed as

$$f_v = \frac{4\pi}{3}\sum_i N_i R_i^3, \tag{21}$$

with N_i being the number density of class i.

TABLE II The material parameters for GP zone evolution modeling, and they are mostly from Ref. 15.

Parameters	Value
Interfacial energy γ	0.01 J/m^2
Nucleation site density N_0	1×10^{-28}/m^3
Molar volume of the precipitate V_m	7×10^{-6} m^3/mol
Maximum radius for the precipitate size distribution	2×10^{-8} m
Lattice parameter a	4.05×10^{-10} m
Mg composition in precipitate c_p	0.33
Pre-exponential coefficient D_0	4.04×10^{-12} m^2/s
Activation energy of diffusion Q_d	31 000 J/mol

Table II lists the parameters for modeling the GP zone evolution. Using these parameters, the radius and volume fraction of GP zones can be correctly predicted during the experiment such as that shown in Ref. 15. The results of this work can be seen in Fig. 5. Since the cooling rate in Fig. 3 is in the range of quenching problem in Ref. 15 these parameters are suitable in this study. Figure 5(a) plots the evolution of the GP zone radius, where the radius between simulation and experiment is in good agreement below 250 °C. Above 250 °C, both simulation and experiment in Fig. 5(b) show that the GP zone volume fraction is close to zero. The radius of the GP zone above 250 °C cannot be found in experiment because of zero volume fraction, while simulation can still predict the theoretical radius if the GP zone exists. Below 250 °C, the volume fraction of GP zones increases and reaches about 5% in both simulation and experiment. Similar to Ref. 15, the volume fraction prediction in simulation shows the right trend, and the slope of the curve and the magnitudes can be slightly different from experiment. This may be the evidence for future improvement of the model or there may be some improvement in the accuracy of the experimental SAXS data.

C. Natural aging

Below 100 °C or at room temperature, the precipitation process occurs very slowly because first the solute concentrations of Mg and Zn are low and the diffusion rate of Mg and Zn is slow at the low temperature. During natural aging, GP zones act to homogeneously nucleate into η'. η' may also have transformed into η, and this is considered in this study for simplicity. In this natural aging process, the temperature is constant. In the KWN theory, if the temperature is a constant, the precipitate nucleates in the equilibrium state and will not grow.

The critical radius of nucleation R^*[25] may be defined as

$$R^* = -\frac{2\gamma V_m}{\Delta G_V} = \frac{2\gamma V_m}{R_g T\ ln(\bar{C}/C_e)}. \tag{22}$$

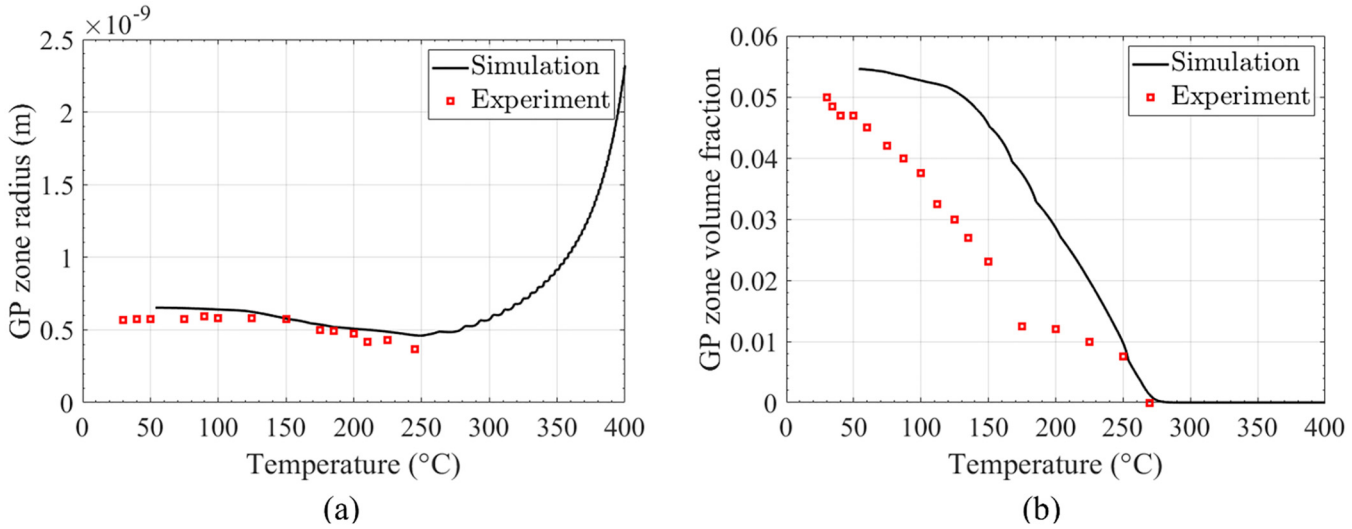

FIG. 5. Model results of GP zone precipitation during fast quenching process, compared with experiment result in Ref. 15. (a) GP zone radius and (b) GP zone volume fraction.

where $\bar{C}$ is the mean solute Mg content in the matrix, γ is the particle–matrix interfacial energy, ΔG_V is the change in Gibbs free energy, C_e is the equilibrium Mg concentration in the matrix, and R_g is the gas constant. $\bar{C}$ is a very small value after the cooling process. Multiple GP zones nucleate into one large particle of η'. It is reasonable to consider $\bar{C}$ of Mg in the solution as a constant during aging since Mg diffuses much slower than Zn, while Zn content may vary. In this sense, η' radius can be considered as a constant based on Eq. (22). This is also found from our TEM image, and in different zones, the size of η' due to natural aging is very similar.

Since the temperature is constant, the GP zones to η' transition is mainly determined by time. It is common to assume the power law between the concentration of GP zones and the main variable t as in Ref. 29. In this study, the following power law is used:

$$c_{\eta'} = \left(c_{GPZ} - c_0 - c_{\eta'}\right)^n \cdot \left(\frac{\Delta G}{q}\right)^m \cdot t^p = \left(c_{GPZ} - c_0 - c_{\eta'}\right)^n \cdot K \cdot t^p, \tag{23}$$

In Eq. (23), $(c_{GPZ} - c_0 - c_{\eta'})^n$ means that the transformation rate increases with the parent phase (GP zones) content c_{GPZ} and decreases with the product phase (η') content $c_{\eta'}$ and c_0 is a threshold for this phase transformation.[29] $K = \Delta G/q$ is the unitless change in the Gibbs free energy determining the transformation rate. In this study, the parameters, $n = 2.8$, $K = 5$, $c_0 = 0.01$, and $p = 0.01$ are used.

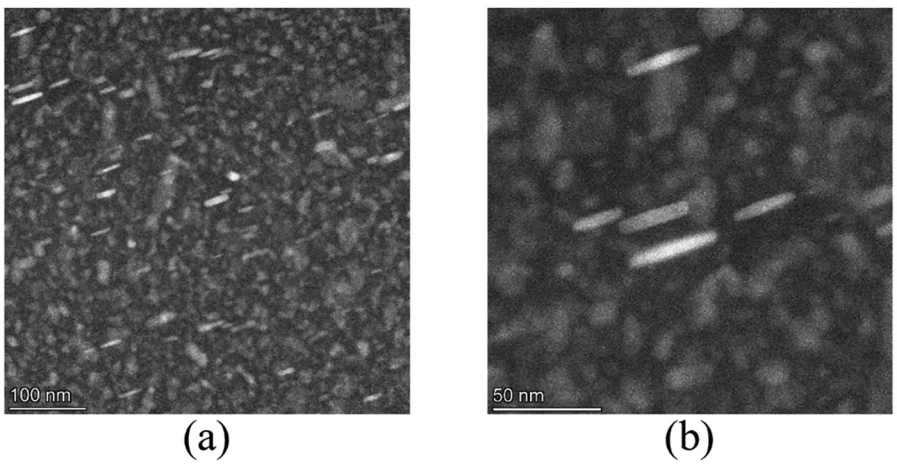

FIG. 6. TEM scan image for AA 7050-T7451 base material. (a) shows that the precipitates are randomly distributed in the matrix and (b) is a more magnified image showing the shape of the precipitates.

V. SIMULATION RESULTS ON PRECIPITATION EVOLUTION FOR THE HOLE REPAIR

A. Modeling precipitates η dissolution and heterogeneous nucleation

As shown in Fig. 6, the η precipitate is homogeneously distributed in the matrix, and has either a cigar or platelet shape. The volume fraction and radius of η can be obtained from the intensity in the SAXS data. In this modeling study, the base material contains 4.1% η in volume fraction and the average of size corresponding to a spherical shape is 6.3 nm, which is consistent with the TEM of the AA7050 -T7451 base material in Fig. 6. Another model input is the grain boundary area A_{GB} per grain and the grain volume V_{Grain} per grain, which can be obtained from our dynamic recrystallization model or from the EBSD data, as shown in Fig. 7. In this study, $A_{GB} = 1200\,\mu\text{m}^2$, $V_{\text{Grain}} = 3000\,\mu\text{m}^3$, and the average grain radius is $\sim 10\,\mu$m.

Figure 8 plots the volume fraction (a) and average radius (b) of the η phase in the matrix during the heating process. The received base material has 4.1% η. At the time around 50 s, the temperature reaches 250 °C in Fig. 3, and the temperature is high enough to cause the dissolution of η, as shown in Fig. 8(a). When the temperature reaches 425 °C at time $t = 115$ s, the entire η phase dissolves into the solution. This is consistent with the η phase solvus temperature of ~425 °C calculated from thermodynamics using JMatPro software.[19] The initial average radius of the η phase is 6.3 nm in Fig. 8(b), and it decreases to 2 nm as the number of precipitate densities goes to zero $t = 120$ s. GP zone precipitation is not considered in the heating process for two reasons: first, before the dissolution of η, there is a very low solute content for GP zone nucleation, and second, when the dissolution of η occurs, the temperature is already above the GP zone solvus temperature.

The volume fraction of the heterogeneously nucleated η phase at the grain boundary is shown in Fig. 8(c). Initially, it cannot nucleate due to the low temperature and the low solute content around the grain boundary. At the time around 50 s, heterogeneous nucleation starts and reaches 0.5% at the time around 80 s. Continuously increasing the temperature to 350 °C and above also leads to the dissolution of the η phase at the grain boundary, and at 106 s, all the heterogeneous η phase dissolves into solution. At the initial cooling time and temperature above 250 °C, the heterogeneous η phase reappears. This is the reason why active cooling could affect the heterogeneous nucleation. It is found in Fig. 8(d) that the heterogeneous η phase can be large ~40 nm, which is consistent with our findings in the TEM of the repaired material shown in Fig. 9. As the radius of precipitate increases, the yield strength of the material decreases. Fine precipitates rather than large heterogeneous precipitates are preferred for high material performance.

B. Modeling GP zone evolution during cooling

With the dissolution of η particles, the concentrations of Mg and Zn in solution increase. In the cooling process, the GP zone nucleation occurs when the temperature is below the GP zone solvus temperature of 250 °C in Fig. 10. Since the interfacial energy between the GP zone and the solution is low, small-sized GP zones can be formed in the very short period of time where the temperature is between 100 and 250 °C. As shown in Fig. 10, the particle fraction of GP zones reaches 7.3% and has a small radius of 1.22 nm. Such fine GP zones also form fine precipitates of the η' phase. The validation of GP zone modeling is discussed in Sec. IV B.

C. Modeling GP zone and η' evolutions during natural aging

Natural aging plays an important role in AA 7050, and typically the material strength increases during this process. This is because the GP zones can form fine and more stable phases that have less coherence with the solution, and further provide resistance to dislocation slip and precipitate hardening. Figure 11 shows

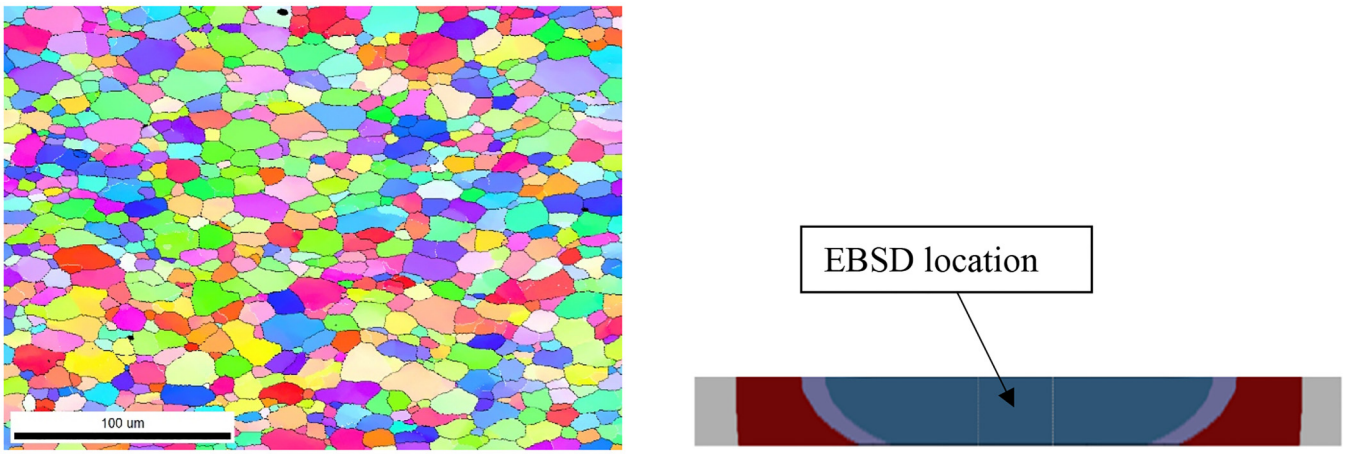

FIG. 7. EBSD image (a) is taken from the middle of deposited material (b). This analysis was performed using a Zeiss LEO 1550 field-emission SEM (Wetzlar, Germany) equipped with an Oxford Nordlys detector.

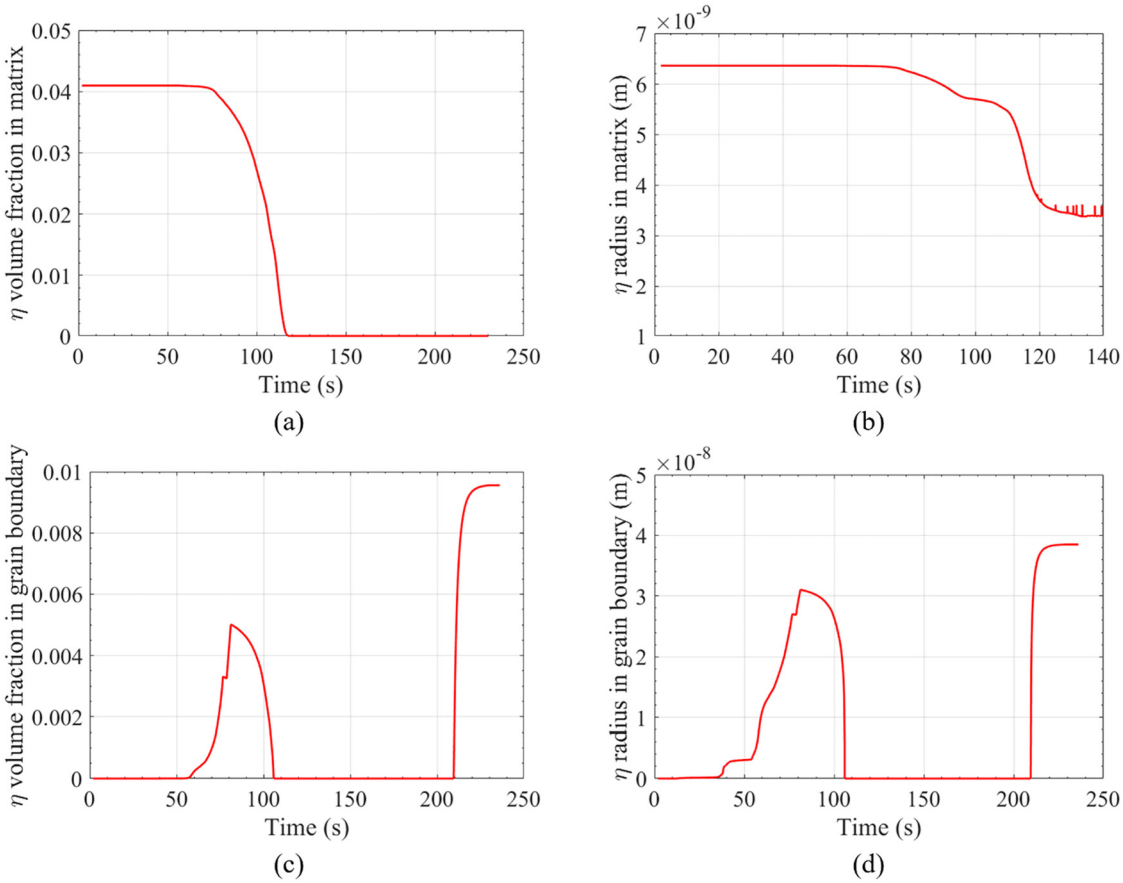

FIG. 8. Volume fraction (a) and (c) and average radius (b) and (d) of the η phase. The homogeneously distributed η phase in the matrix in (a) and (b), and the heterogeneously distributed η in the grain boundaries in (c) and (d).

the evolution of the GP zone and η', and the time scale is days instead of seconds as shown in the previous two stages. The phase transformation from GP zones to η' occurs rapidly during the first seven days, and then becomes more stable with an increasing time. On the seventh day, η' is 4% and GP zones are 3.5%. Both are very fine in size. In Sec. V A, we explain theoretically that the size of η' may be considered as constant. This is consistent with our TEM images in Fig. 12. The average length of the needle may be 8 nm but the other two directions may be only 1–2 nm. It may be converted to a radius of ~2.5 nm in a spherical shape with the same volume.

D. Precipitate effects in material performance after natural aging

After seven days of aging at room temperature, η' precipitates in the matrix are ~2.5 nm in radius and 4% in volume fraction, and GP zones are 1.22 nm and 3.5%. In addition, there are 0.96% heterogeneous η with a radius of ~40 nm, compared with the base material of the η phase of 4.1% and 6 nm in radius. Obviously, GP zones and η' in the stir zone have a much finer size than the base material, and the volume fraction of the GP zones plus η' is larger than the base material precipitates. While overgrown precipitates at the grain boundary can reduce material performance, there is only less than 1% volume fraction. Therefore, we expect higher strength in stir zone materials than the base material. Fatigue indicator parameters (FIPs) serve as surrogate measures of the driving force to form and grow microstructurally small cracks within and across grains. These FIPs correlate with the number of cycles to form a fatigue crack with a length on the order of the damage process zone over which they are averaged.[30] Typically, a smaller FIP leads to higher fatigue life for crack initiations, which contributes the majority of fatigue life for low cycle fatigue tests. Various fatigue parameter indicators (FIPs) have been defined and used for fatigue correlations or prediction. Castelluccio and McDowell[31] investigated a transgranular version of the FIP_α defined by

$$FIP_\alpha = \frac{\Delta\gamma_p^\alpha}{2}\left|1 + k\frac{\sigma_n^\alpha}{\sigma_y}\right|, \tag{24}$$

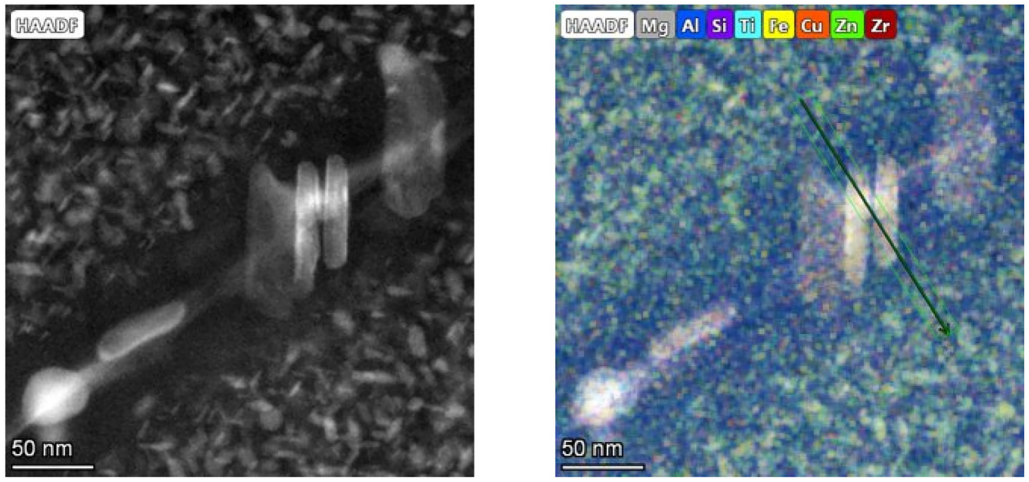

FIG. 9. TEM image about the grain boundary precipitate η in hole repair and the location is the same as in the EBSD image shown in Fig. 7(b). Transmission electron microscopy (TEM) characterization was performed on an FEI Titan (Waltham, USA). TEM samples were made by cutting 3 mm diameter cylinders via electric discharge machining (EDM), and then the cylinders were sectioned and polished to 100 μm thickness and twin jet electropolished with an 80 wt. % methanal–20 wt. % HNO_3 electrolyte at −20 °C.

where $\Delta\gamma_p^\alpha$ is the range of cyclic plastic shear strain on the αth slip system, σ_n^α is the peak stress normal to this slip plane α. They showed a close correlation between FIP_α and the crack tip displacement range (ΔCTD), which is often used to quantify fatigue crack formation and growth driving forces[30–32]) for cracks in homogeneous single crystals and cracks lying at the interface of a slip band in a single crystal. AA 7050 is an Al–Zn–Mg–Cu alloy with the small addition of Zr. AA 7075 is also an Al–Zn–Mg–Cu alloy that has slightly less Zn, slightly more Cu, and uses chromium instead of Zr for the dispersoid particle. AA 7075 and AA 7050 have very similar elasticity and plasticity performances. Usually, k is around 1 for most materials, while for AA 7075, it is found that k is 10.[30]

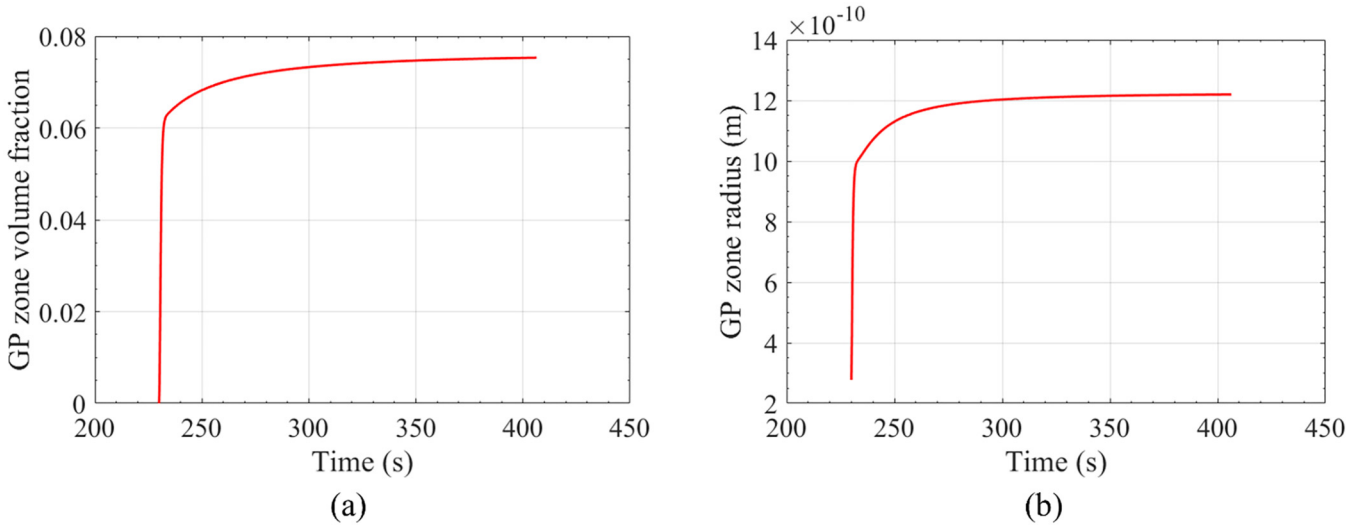

FIG. 10. GP zone evolution during cooling. (a) Volume fraction and (b) average radius of GP zones.

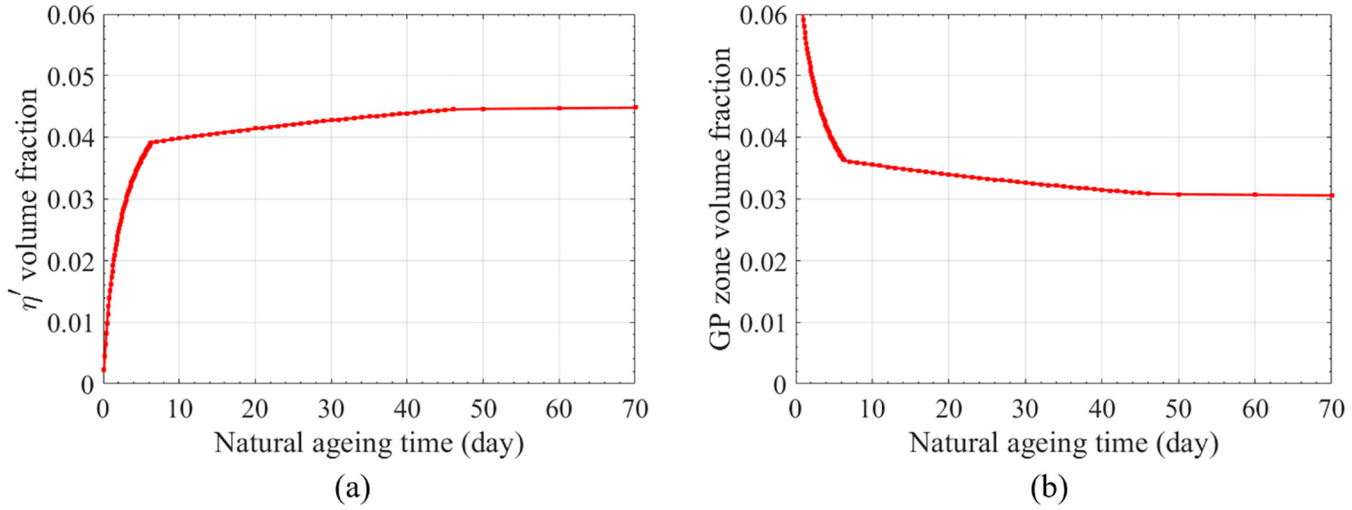

FIG. 11. The evolution of (a) η' and (b) GP zone during natural aging.

This means the FIP is mostly determined by the yield strength of materials with weaker dependences on the plastic deformation compared to materials with $k = 1$ as shown in Eq. (24). The precipitates of the hole repaired material create high strength in stir zone materials and low plastic strain $\Delta\gamma_p^{\alpha}$, which further leads to a small FIP_{α} and an increased fatigue life based on Eq. (24) as found in Ref. 8. Another possible explanation for a better fatigue life of hole repaired samples than the pristine ones is that Fe-rich constituent particles break into small particles due to high shear force in AFSD, and the crack initiation does not start at the Fe-rich constituent particles after AFSD.[8] We noted that the experimental fatigue results exhibited significant scatter for AA 7075 wrought and AFSD heat treated (HT) repaired plate in Ref. 12, which could also be found in our AA 7050 AFSD repaired and pristine materials in Ref. 8 while there is no heat treatment on repaired materials. In addition, the AA 7075 HT repaired materials showed a slightly lower fatigue life than the base materials, which is different from the current hole repair coupons with better fatigue life. One reason as identified in Ref. 12 is that carbon impurities can reduce the crack initiation life. As in Fig. 2, we deposited much less material compared to the case in Ref. 12, and therefore the carbon percentage in our coupons is much lower. The carbon impurity can be a severe issue when we manufacture components in a large scale via AFSD. Another reason is that the material experiences a completely different thermal history, and the precipitation evolution is completely different. From TEM images and simulation results, we obtained much finer precipitates than the pristine materials.

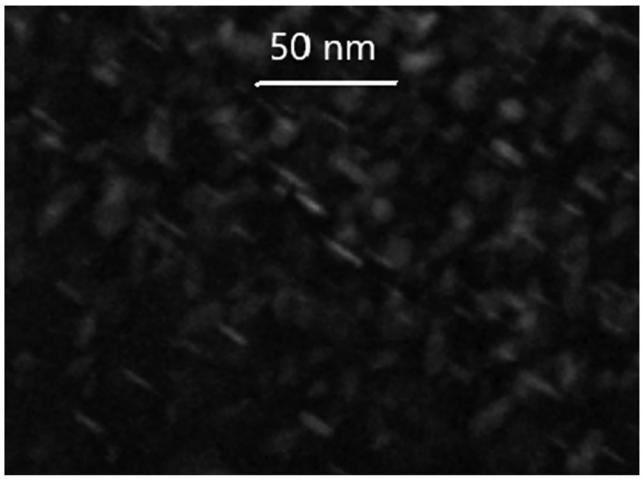

FIG. 12. Needle-like of η' during natural aging in hole repair in the stir zone and the location is the same as in EBSD image as shown in Fig. 7(b).

VI. CONCLUSIONS

In this paper, a multi-stage precipitation model is developed to predict the precipitation evolution and explain the high fatigue performance of deposited aluminum alloy 7050 (AA 7050) utilized in an additive friction stir deposition (AFSD) enabled hole repair.

When the temperature reaches 250 °C in the heating process, fast dissolution of η in the matrix occurs. When the temperature reaches 425 °C, the entirety of η in the matrix dissolves into solution. The volume fraction and radius of the heterogeneously nucleated η phase at the grain boundary are also modeled. Initially, η cannot nucleate due to the low temperature and the low solute content around the grain boundary. At the time around 50 s, heterogeneous nucleation starts and reaches 0.5% at the time around 80 s. Continuously increasing the temperature to 350 °C and above also leads to the dissolution of the η phase at the grain boundary, and at 105 s, all the heterogeneous η phase dissolves into solution.

At the initial cooling time and temperature above 250 °C, the heterogeneous η phase reappears at the grain boundary. The heterogeneous η phase can be large, ~40 nm from simulations, which is consistent with our findings in the TEM image. With the dissolution of η particles in the matrix, the Mg and Zn in the solution increase. In the cooling process, we have GP zone nucleation when the temperature is below the GP zone solvus temperature of 250 °C. Since the interfacial energy between the GP zone and the solution is small, small GP zones can be formed in the short period of time while cooling between 250 and 100 °C. The volume fraction of GP zones reaches 7.3% and has a small radius of 1.22 nm at the end of the cooling process.

Fine GP zones form fine precipitates of the η' phase during the natural aging process. The evolution of the GP zone and η' occurs over the course of days and weeks as opposed to the seconds scale considered with typical evolution. The phase transformation from GP zones to η' occurs rapidly during the first seven days, and then becomes more stable with increasing time. On the seventh day, η' is 4% volume fraction and GP zones are 3.5% volume fraction. Both are very fine in size, which is consistent with our TEM images and SAXS data in literature.[15]

The GP zones and η' in the stir zone have a much finer size than the base material, and the volume fraction of the GP zones plus η' is larger than the base material precipitates. These precipitates in hole repaired material favor a high strength and low plastic strain, which lead to a high fatigue life,[8] which provides an alternative explanation for the fatigue performance in Ref. 8. The obtained results contribute to the understanding of the strengthening mechanism and should be beneficial for tailoring the thermal control for achieving a microstructure with optimum performances.

ACKNOWLEDGMENTS

This work is supported by the U.S. Naval Air Systems Command (NAVAIR) Funding Contract Nos. N68335-21-C-0504, N68335-22-G-0006, and N68335-23-C-0115. This support is gratefully acknowledged. The discussion with Dr. Hang Yu from Virginia Tech is greatly appreciated.

AUTHOR DECLARATIONS

Conflict of Interest

The authors have no conflicts to disclose.

Author Contributions

Bill Feng: Conceptualization (lead); Data curation (lead); Formal analysis (lead); Investigation (lead); Methodology (lead); Validation (lead); Visualization (lead); Writing – original draft (lead); Writing – review & editing (equal). **Manoj R. Rajanna:** Conceptualization (supporting); Formal analysis (supporting); Investigation (supporting); Writing – review & editing (supporting). **Jim Lua:** Conceptualization (equal); Methodology (equal); Project administration (equal); Resources (equal); Supervision (equal). **Greg Hahn:** Conceptualization (equal); Investigation (equal); Methodology (equal); Writing – review & editing (equal). **Kendall Knight:** Conceptualization (equal); Methodology (equal); Writing – review & editing (equal). **Gabriel Murray:** Conceptualization (equal); Resources (equal); Supervision (equal). **Alan Timmons:** Conceptualization (equal); Resources (equal); Supervision (equal). **Nam Phan:** Conceptualization (equal); Resources (equal); Supervision (equal).

DATA AVAILABILITY

The data that support the findings of this study are available from the corresponding author upon reasonable request.

REFERENCES

[1]J. Telesman, "Review of the effects of micro structure on fatigue in aluminum alloys," NTRS—NASA Technical Memorandum No. 83626 (1984).
[2]H. Z. Yu and G. D. Hahn, "Potential and challenges for large-scale near-net-shaping of 7xxx aerospace grade aluminum via additive friction stir deposition," Mater. Lett. X **19**, 100217 (2023).
[3]O. G. Rivera, P. G. Allison, J. B. Jordon, O. L. Rodriguez, L. N. Brewer, Z. McClelland, W. R. Whittington, D. Francis, J. Su, R. L. Martens, and N. Hardwick, "Microstructures and mechanical behavior of inconel 625 fabricated by solid-state additive manufacturing," Mater. Sci. Eng. A **694**, 1–9 (2017).
[4]R. Joey Griffiths, D. T. Petersen, D. Garcia, and H. Z. Yu, "Additive friction stir-enabled solid-state additive manufacturing for the repair of 7075 aluminum alloy," Appl. Sci. **9**(17), 3486 (2019).
[5]D. Z. Avery, B. J. Phillips, C. J. T. Mason, M. Palermo, M. B. Williams, C. Cleek, O. L. Rodriguez, P. G. Allison, and J. B. Jordon, "Influence of grain refinement and microstructure on fatigue behavior for solid-state additively manufactured Al-Zn-Mg-Cu alloy," Metall. Mater. Trans. A **51**(6), 2778–2795 (2020).
[6]J. Glenn, L. Dean, A. Wright, and Y. Hovanski, "Closed-loop PID temperature control of additive friction stir deposition," in *Friction Stir Welding and Processing XII. TMS 2023*, The Minerals, Metals & Materials Series, edited by Y. Hovanski, Y. Sato, P. Upadhyay, A. A. Naumov, and N. Kumar (Springer, Cham, 2023).
[7]G. D. Hahn, K. P. Knight, N. Gotawala, and H. Z. Yu, "Additive friction stir deposition of AA7050 achieving forging-like tensile properties," Mater. Sci. Eng. A **896**, 146268 (2024).
[8]G. Hahn, K. Knight, and H. Yu, "Solid-state structural repair of corroded fastener holes in high strength aluminum via additive friction stir deposition" (submitted for publication, 2024).
[9]M. Dixit, R. S. Mishra, and K. K. Sankaran, "Structure-property correlations in Al 7050 and Al 7055 high-strength aluminum alloys," Mater. Sci. Eng. A **478**(1–2), 163–172 (2008).
[10]C. J. T. Mason, D. Z. Avery, B. J. Phillips, J. B. Jordon, and P. G. Allison, "Strain rate dependent plasticity model for precipitate hardened aerospace aluminum alloy produced with solid-state additive manufacturing," J. Dyn. Behav. Mater. **8**(2), 214–230 (2022).
[11]N. I. Palya, K. Fraser, N. Zhu, J. B. Hoarston, K. Doherty, P. G. Allison, and J. B. Jordon, "Microstructure prediction from smooth particle hydrodynamics process simulations of additive friction stir deposition," Metall. Mater. Trans. A **55**(9), 3601–3616 (2024).
[12]D. Z. Avery, C. E. Cleek, B. J. Phillips, M. Y. Rekha, R. P. Kinser, H. M. Rao, L. N. Brewer, and P. G. Allison, "Evaluation of microstructure and mechanical properties of Al-Zn-Mg-Cu alloy repaired via additive friction stir deposition," J. Eng. Mater. Technol. **144**(3), 031003 (2022).
[13]N. I. Palya, K. A. Fraser, Y. Hong, N. Zhu, M. B. Williams, K. Doherty, P. G. Allison, and J. B. Jordon, "Multi-Physics approach to predict fatigue behavior of high strength aluminum alloy repaired via additive friction stir deposition," Integr. Mater. Manuf. Innov. **12**(4), 441–455 (2023).
[14]R. Wagner and R. Kampmann, *Materials Science and Technology—A Comprehensive Treatment* (Wiley-VCH, New York, 1991).
[15]P. Schloth, A. Deschamps, C. A. Gandin, and J. M. Drezet, "Modeling of GP (I) zone formation during quench in an industrial AA7449 75 mm thick plate," Mater. Des. **112**, 46–57 (2016).

[16]P. Schloth, J. N. Wagner, J. L. Fife, A. Menzel, J. M. Drezet, and H. Van Swygenhoven, "Early precipitation during cooling of an Al-Zn-Mg-Cu alloy revealed by *in situ* small angle x-ray scattering," Appl. Phys. Lett. **105**(10), 101908 (2014).
[17]N. Kamp, A. Sullivan, and J. D. Robson, "Modelling of friction stir welding of 7xxx aluminium alloys," Mater. Sci. Eng. A **466**(1–2), 246–255 (2007).
[18]N. Kamp, A. P. Reynolds, and J. D. Robson, "Modelling of 7050 aluminium alloy friction stir welding," Sci. Technol. Weld. Joining **14**(7), 589–596 (2009).
[19]N. Kamp, A. Sullivan, R. Tomasi, and J. D. Robson, "Modelling of heterogeneous precipitate distribution evolution during friction stir welding process," Acta Mater. **54**(8), 2003–2014 (2006).
[20]M. J. Starink, A. Deschamps, and S. C. Wang, "The strength of friction stir welded and friction stir processed aluminium alloys," Scr. Mater. **58**(5), 377–382 (2008).
[21]Y. Zhang, D. Pelliccia, B. Milkereit, N. Kirby, M. J. Starink, and P. A. Rometsch, "Analysis of age hardening precipitates of Al-Zn-Mg-Cu alloys in a wide range of quenching rates using small angle x-ray scattering," Mater. Des. **142**, 259–267 (2018).
[22]M. Dumont, A. Steuwer, A. Deschamps, M. Peel, and P. J. Withers, "Microstructure mapping in friction stir welds of 7449 aluminium alloy using SAXS," Acta Mater. **54**(18), 4793–4801 (2006).
[23]X. Li, M. Rajanna, J. Lua, A. Timmons, G. Murray, N. Phan, and R. Eberheim, "Computational fluid dynamics simulation for additive friction stir deposition of aluminum alloy," in *The Conference of "Manufacturing Technology and Processing*, SKU No. F-0079-2023-18105 (2023), 9 p.
[24]C. B. Fuller, M. W. Mahoney, M. Calabrese, and L. Micona, "Evolution of microstructure and mechanical properties in naturally aged 7050 and 7075 Al friction stir welds," Mater. Sci. Eng. A **527**(9), 2233–2240 (2010).
[25]C. A. Gandin and A. Jacot, "Modeling of precipitate-free zone formed upon homogenization in a multi-component alloy," Acta Mater. **55**(7), 2539–2553 (2007).
[26]G. Sha and A. Cerezo, "Early-stage precipitation in Al-Zn-Mg-Cu alloy (7050)," Acta Mater. **52**(15), 4503–4516 (2004).
[27]H. B. Aaron and H. I. Aaronson, "Growth Of grain boundary precipitates in Al-4% Cu By interfacial diffusion*," Acta Metall. **16**, 789–798 (1968).
[28]R. A. Carolan and R. G. Faulkner, "Grain boundary precipitation of M23C6 in an austenitic steel," Acta Metall. **36**(2), 257–266 (1988).
[29]F. L. Addessio, D. J. Luscher, M. J. Cawkwell, and K. J. Ramos, "A single-crystal model for the high-strain rate deformation of cyclotrimethylene trinitramine including phase transformations and plastic slip," J. Appl. Phys. **121**(18), 185902 (2017).
[30]K. S. Stopka, M. Yaghoobi, J. E. Allison, and D. L. McDowell, "Effects of boundary conditions on microstructure-sensitive fatigue crystal plasticity analysis," Integr. Mater. Manuf. Innov. **10**(3), 393–412 (2021).
[31]G. M. Castelluccio and D. L. McDowell, "Assessment of small fatigue crack growth driving forces in single crystals with and without slip bands," Int. J. Fract. **176**(1), 49–64 (2012).
[32]K. S. Stopka and D. L. McDowell, "Microstructure-sensitive computational multiaxial fatigue of Al 7075-T6 and duplex Ti-6Al-4V," Int. J. Fatigue **133**, 105460 (2020).